

Bidirectional motion of droplets on gradient liquid infused surfaces

Muhammad Subkhi Sadullah¹, Gaby Launay², Jayne Parle¹, Rodrigo Ledesma-Aguilar ^{2,4}, Yonas Gizaw³, Glen McHale ^{2,4}, Gary George Wells^{2,4} & Halim Kusumaatmaja ¹✉

The current paradigm of self-propelled motion of liquid droplets on surfaces with chemical or topographical wetting gradients is always mono-directional. In contrast, here, we demonstrate bidirectional droplet motion, which we realize using liquid infused surfaces with topographical gradients. The deposited droplet can move either toward the denser or the sparser solid fraction area. We rigorously validate the bidirectional phenomenon using various combinations of droplets and lubricants, and different forms of structural/topographical gradients, by employing both lattice Boltzmann simulations and experiments. We also present a simple and physically intuitive analytical theory that explains the origin of the bidirectional motion. The key factor determining the direction of motion is the wettability difference of the droplet on the solid surface and on the lubricant film.

¹Department of Physics, Durham University, South Road, Durham DH1 3LE, UK. ²Smart Materials and Surfaces Laboratory, Northumbria University, Newcastle upon Tyne NE1 8ST, UK. ³The Procter and Gamble Co., Mason Business Center, 8700 South Mason-Montgomery Road, Mason, OH, USA. ⁴Present address: School of Engineering, The University of Edinburgh, Kings Buildings, Edinburgh EH9 3FB, UK. ✉email: halim.kusumaatmaja@durham.ac.uk

Controlling droplet motion on a solid surface is important for a wide range of applications, from droplet microfluidics to water harvesting and self-cleaning surfaces^{1–6}. Among the various approaches to induce motion, a good passive strategy is to introduce a wetting gradient on the solid surface, as this does not require energy to be provided continuously to the system. Such spontaneous motion has been extensively investigated for binary fluid systems under a variety of wetting gradients, including due to variations in surface chemistry^{7,8}, topography^{9–11} and elasticity¹².

More recently, there has been a growing interest to study droplet self-propulsion on liquid-infused surfaces^{13–15}. These are composite substrates constructed by infusing rough, textured or porous materials with wetting lubricants^{16–18}, which are known for their ‘slippery’ properties. They have also been shown to exhibit a number of other advantageous surface properties, including anti-biofouling, anti-icing and self-healing^{19–21}. Importantly, in all cases reported to date, including existing works on liquid-infused surfaces, droplet motion on surfaces with texture/topographical gradients is always uni-directional towards the denser solid fraction area, where the textures are more closely packed.

In contrast, here we will demonstrate a bidirectional droplet motion. The presence of the lubricant on liquid-infused surfaces can be exploited for a novel self-propulsion mechanism, in which the droplet may have preferential wetting on either the denser or the sparser solid fraction area. We structure our contribution as follows. First, we develop an analytical theory that elaborates how topographical gradient gives rise to the driving force that can propel droplets toward two possible directions. The spontaneous bidirectional motion depends on the combination of the solid, lubricant and liquid droplet, and it can occur as long as the lubricant does not fully wet the solid both in presence of the gas and the liquid droplet surroundings. We then verify our theory using both lattice Boltzmann simulations and experiments. We demonstrate this phenomenon can be observed using various liquid combinations for the droplets and lubricants, as well as for different forms of structural gradients.

Results

The origin of the driving force. When a liquid droplet is placed on a homogenous solid surface, it stays stationary because the surface tension force pulls the base of the droplet equally in the radial direction²². This force balance is broken when the wettability of one side of the droplet is different from the other, resulting in a spontaneous droplet motion towards the more wettable region of the solid²³.

On liquid-infused surfaces, the apparent contact angle of a droplet depends on the surface tensions and the intrinsic contact angles of all fluids involved in the system^{24–26}. This rich interplay makes it much less trivial to predict the direction of droplet motion when there is a topographical gradient. Figure 1 provides an example of the bidirectional motion. In Fig. 1(a), when a structured substrate with a topographical gradient is infused with an ionic liquid, a water droplet placed on the surface moves toward the sparser solid fraction area. In contrast, when the same substrate is infused with Krytox oil, the water droplet moves toward the denser solid fraction area, as shown in Fig. 1(b). To understand this bidirectional droplet motion, we need to break down the contributing surface tension forces.

Consider a liquid droplet placed on top of a liquid-infused surface with topographical gradient, as shown in Fig. 2(a). The substrate is set horizontally such that gravity does not play a role. For convenience, we use the subscripts w, o, a and s to refer to the droplet, infusing lubricant, air and solid phases, respectively.

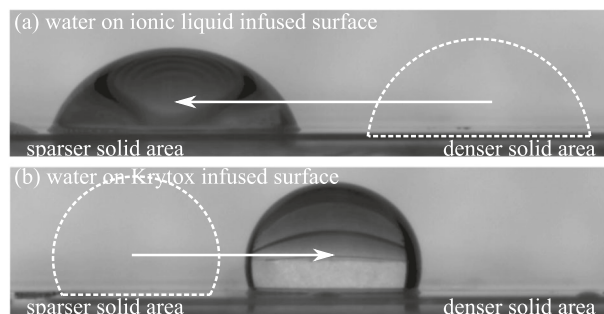


Fig. 1 Spontaneous droplet motion on liquid-infused surfaces with topographical gradient. **a** Water droplet on ionic liquid-infused surface moves toward sparser solid area, while for **b** Krytox-infused surface, the water droplet moves toward denser solid area. For the two cases, only the lubricant is changed. The dashed shapes represent the initial position of the droplets, and the arrows the direction of motion of the droplets.

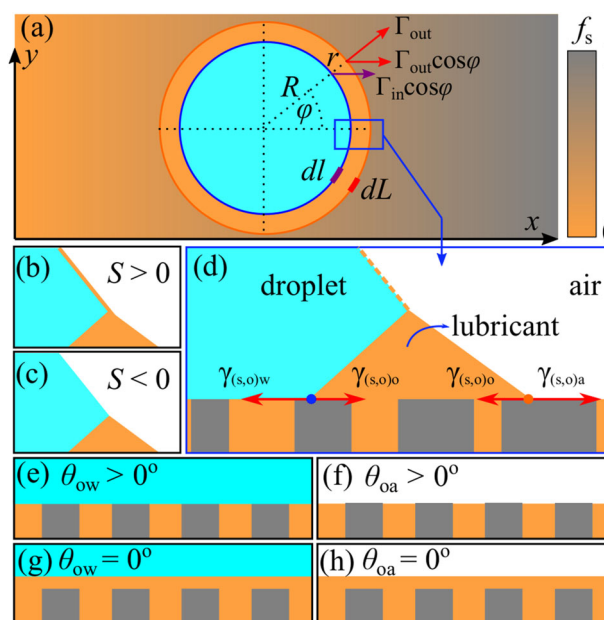


Fig. 2 Illustration of a droplet on a liquid-infused surface with topographical gradient. **a** The droplet and lubricant meniscus are represented by the turquoise and orange discs, respectively. The greater solid fraction (f_s) area is indicated by the darker colour. R and r are the droplet base radius and meniscus width, respectively. Γ_{out} and Γ_{in} are the surface tension forces per unit length that act on the outer and inner contact lines, with ϕ the angle in the azimuthal direction, and dL and dL the infinitesimal length of the inner and the outer contact lines respectively. **b, c** Depending on the sign of the spreading parameter S , the lubricant may encapsulate the droplet. **d** Magnification of the meniscus area (side-view). The dashed line at the droplet-air interface indicates the possibility of lubricant encapsulation, while the grey rectangles represent the surface topography, infused with lubricant (orange). The red arrows indicate the relevant interfacial tensions $\gamma_{(s,o)\alpha}$ of the composite solid-lubricant surface with fluid phase α . **e–h** Possible wetting states depending on the lubricant contact angle on the solid surface in the droplet (θ_{ow}) and air (θ_{oa}) environments.

Furthermore, we introduce the spreading parameter¹⁸,

$$S = \gamma_{wa} - \gamma_{oa} - \gamma_{ow}, \quad (1)$$

with $\gamma_{\alpha\beta}$ the interfacial tension between phases α and β . The droplet is encapsulated by the lubricant when $S > 0$ ^{18,25,27}, see

Fig. 2(b). For $S < 0$, the droplet is not encapsulated, as illustrated in Fig. 2(c).

We will now argue that liquid-infused surfaces can be considered as composite surfaces of solid and lubricant, with fractions of f_s and $(1 - f_s)$, respectively. Therefore, the *composite* interfacial tension of the liquid-infused surface with phase α is $\gamma_{(s,o)\alpha} \equiv f_s \gamma_{s\alpha} + (1 - f_s) \gamma_{o\alpha}$. Letting the solid fraction f_s vary in the x -direction only leads to the interfacial tensions (Fig. 2(d))

$$\gamma_{(s,o)w} \equiv f_s(x) \gamma_{sw} + (1 - f_s(x)) \gamma_{ow}, \quad (2)$$

$$\gamma_{(s,o)o} \equiv f_s(x) \gamma_{so} + (1 - f_s(x)) \gamma_{oo} = f_s(x) \gamma_{so}, \quad (3)$$

$$\gamma_{(s,o)a} \equiv f_s(x) \gamma_{sa} + (1 - f_s(x)) \gamma_{oa}. \quad (4)$$

The relevant surface tension forces per unit length that pull the droplet in the radial direction are $\Gamma_{in} = \gamma_{(s,o)o} - \gamma_{(s,o)w}$ and $\Gamma_{out} = \gamma_{(s,o)a} - \gamma_{(s,o)o}$ for the inner (droplet–lubricant–composite substrate) and the outer (lubricant–air–composite substrate) contact lines, respectively. As detailed in Supplementary Note 1, we assume that the droplet shape is in quasi-equilibrium, so that the net contributions from the droplet–air, droplet–lubricant and lubricant–air surface tensions go to zero. Indeed, both in the experiments and simulations, only a slight asymmetry in the droplet shapes is observed. Furthermore, since f_s does not vary with y , only the x -component of the forces contributes to the driving force, i.e., $\Gamma_{in} \cos \varphi$ and $\Gamma_{out} \cos \varphi$ (see Fig. 2(a)). The total driving force is thus the sum of these surface tensions integrated over the total perimeters of the inner and outer contact lines,

$$F = \int_l \Gamma_{in} \cos \varphi dl + \int_L \Gamma_{out} \cos \varphi dL. \quad (5)$$

Assuming the droplet base is circular, we can express $dl = R d\varphi$ and $dL = (R + r) d\varphi$. In this case, the terms without $f_s(x)$ vanish when the driving force is integrated over the contact line since $\oint \cos \varphi dL = 0$ and $\oint \cos \varphi dl = 0$. Moreover, if the meniscus is much smaller than the droplet base radius, we can approximate $R + r \approx R$, and thus, $dl = dL = R d\varphi$. The finite meniscus size case is described in Supplementary Note 1.

In this vanishing meniscus approximation, we can substitute the definitions of the composite interfacial tensions in Eqs. (2)–(4) to Eq. (5), and write the driving force as

$$F = ((\gamma_{so} - \gamma_{sw} + \gamma_{ow}) + (\gamma_{sa} - \gamma_{so} - \gamma_{oa})) \times \int_{\varphi} f_s(x) R \cos \varphi d\varphi. \quad (6)$$

We have explicitly kept the γ_{so} in the above equation for clarity. In particular, we can simplify Eq. (6) by employing the Young's contact angles of the lubricant in the air and in the droplet phase environment, respectively, defined as $\cos \theta_{oa} = (\gamma_{sa} - \gamma_{so}) / \gamma_{oa}$ and $\cos \theta_{ow} = (\gamma_{sw} - \gamma_{so}) / \gamma_{ow}$. In this case, Eq. (6) becomes

$$F = (\gamma_{ow}(1 - \cos \theta_{ow}) + \gamma_{oa}(\cos \theta_{oa} - 1)) \times \int_{\varphi} f_s(x) R \cos \varphi d\varphi. \quad (7)$$

We can expect spontaneous motion to occur if either the droplet–lubricant–solid line or the air–lubricant–solid contact line is present. This is typically the case when θ_{ow} or θ_{oa} is non-zero¹⁸, as illustrated in Fig. 2(e) and (f), respectively. The driving force ceases ($F = 0$) only if the surface topography is covered by a layer of lubricant everywhere. Thermodynamically, this occurs when the lubricant completely wets the solid surface both in the droplet and air phase environments¹⁸, such that $\theta_{ow} = \theta_{oa} = 0$, as illustrated in Fig. 2(g) and (h), respectively. In addition, the

air–lubricant–solid contact line may also become absent if significant excess lubricant is used.

To determine the direction of droplet motion, we can introduce the droplet–air effective interfacial tension²⁶

$$\gamma_{eff} \equiv \begin{cases} \gamma_{oa} + \gamma_{ow}, & \text{if } S > 0 (\text{lubricant encapsulation}), \\ \gamma_{wa}, & \text{otherwise,} \end{cases}$$

and the following definitions of apparent contact angles

$$\cos \theta_{wa|s}^{eff} \equiv \frac{\gamma_{sa} - \gamma_{sw}}{\gamma_{eff}}, \quad \cos \theta_{wa|o}^{eff} \equiv \frac{\gamma_{oa} - \gamma_{ow}}{\gamma_{eff}}, \quad (8)$$

such that the driving force in Eq. (6) can be written in the following form

$$F = \gamma_{eff} \left(\cos \theta_{wa|s}^{eff} - \cos \theta_{wa|o}^{eff} \right) \int_{\varphi} f_s(x) \cos \varphi R d\varphi. \quad (9)$$

$\theta_{wa|s}^{eff}$ and $\theta_{wa|o}^{eff}$ are defined as the contact angles of the droplet, either encapsulated by lubricant or not, on a smooth solid surface and on the lubricant surface, respectively. When there is no encapsulation, $\gamma_{eff} = \gamma_{wa}$ and hence $\theta_{wa|s}^{eff} = \theta_{wa|s}$, which is the familiar Young's contact angle of a droplet on a smooth solid surface²².

Let us now discuss the terms in Eq. (9). The term under the integral depends on the details of the surface patterning, $f_s(x)$, and it modulates the strength of the driving force. The direction of the driving force is determined only by the sign of the gradient in $f_s(x)$ and by the prefactor

$$\tilde{F} = \left(\cos \theta_{wa|s}^{eff} - \cos \theta_{wa|o}^{eff} \right), \quad (10)$$

which is in fact independent of the surface texture. This has a clear and intuitive physical interpretation: it corresponds to the preferential wetting of the droplet on the region exhibiting the majority of solid or lubricant surface. Without any loss of generality, let us assume that the gradient in $f_s(x)$ is positive, i.e., the solid fraction becomes denser with increasing x . When $\cos \theta_{wa|s}^{eff} > \cos \theta_{wa|o}^{eff}$, the droplet prefers to wet the solid rather than the lubricant. Therefore, the droplet moves toward the solid majority surface (denser solid area). In contrast, when $\cos \theta_{wa|s}^{eff} < \cos \theta_{wa|o}^{eff}$, the droplet moves toward the lubricant majority surface (sparser solid area).

Demonstration of bidirectional motion. To validate the prediction of Eq. (10), we perform both simulations and experiments of droplets moving across liquid-infused surfaces with textural gradients. Supplementary Movies 1, 2 and 3 show the typical droplet motion on linear and stepwise gradients from our experiments. The details of the simulation and experimental methods are provided in the Method section and in Supplementary Methods.

Figure 3(a) shows a phase diagram for the normalised driving force (\tilde{F}), predicted by Eq. (10) (colourmap), and the corresponding droplet motion observed in the numerical simulations and the experiments (symbols). The upper section of the phase map corresponds to an expected driving force directed towards the denser solid regions, while the lower section towards the sparser solid regions. The colour of the symbols represents motion to the denser (blue) or sparser (red) solid fraction area, showing a good agreement between the numerical simulations and the experiments with the theoretical prediction.

Our numerical simulations show that the mechanism leading to bidirectional motion holds and that the relevant control parameter linked to the topography of the solid is the solid fraction f_s . Two major advantages of the numerical simulations

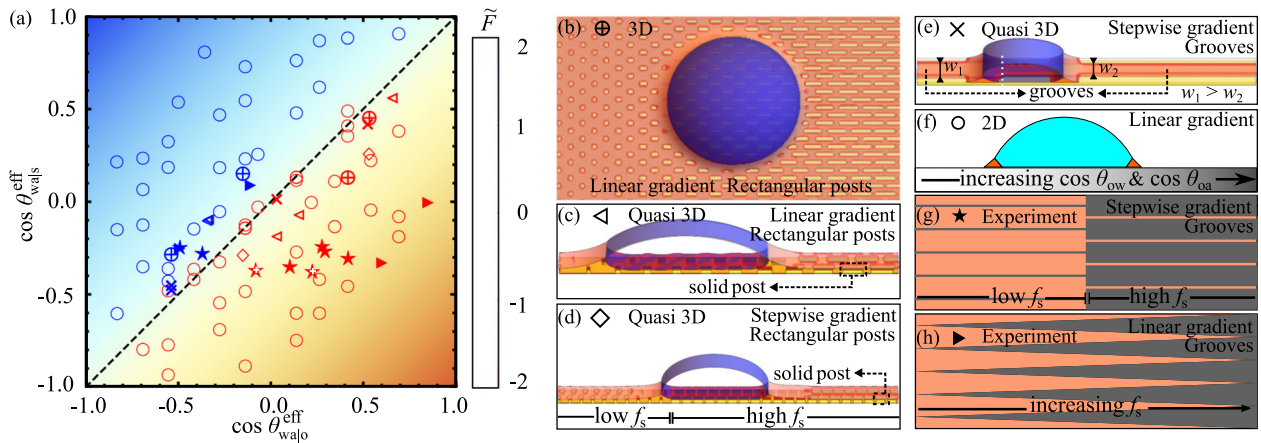


Fig. 3 Confirmation of the bidirectional motion of droplets on liquid-infused surfaces with topographical gradients. **a** The colourmap describes the normalised driving force \tilde{F} provided in Eq. (10), with $\theta_{wal,s}^{eff}$ and $\theta_{wal,o}^{eff}$ the droplet apparent contact angle on a smooth solid surface and on a lubricant surface, respectively. The data points were obtained from simulations and experiments, in which the droplets were observed to move to the solid majority (blue) or the lubricant majority (red) surfaces. The symbols \oplus , \triangleleft , \diamond , \times and \circ are from simulations, where we have used linear gradient of rectangular posts in **b** full 3D and **c** quasi 3D setups, stepwise gradient of **d** rectangular posts and **e** grooves in quasi 3D setups, and **f** 2D setups. Here, the solid and lubricant are coloured in yellow and orange, respectively. The symbols \star and \triangleright are from experiments (the hollow symbols indicate the lubricant encapsulation case). They correspond to **(g)** stepwise gradient and **(h)** linear gradient of grooves. The solid and lubricant are represented in grey and orange, respectively.

are that we are able to systematically explore a wide range of variations in surface tensions and surface topographies. Specifically, we consider three different simulation geometries. First, we use full three-dimensional (3D) simulations with linear gradient of rectangular posts (\oplus , Fig. 3(b)). For the linear gradient, the post length is increased for each subsequent post in the x -direction. Second, we carry out quasi 3D simulations, where a cylindrical droplet and only a period of the surface features in the y direction are used. Here, we employ both a linear gradient of rectangular posts (\triangleleft , Fig. 3(c)), as well as stepwise gradients of rectangular posts (\diamond , Fig. 3(d)) and grooves (\times , Fig. 3(e)). In the case of a stepwise gradient, the substrate is divided into lower and higher f_s regimes. Third, we use two-dimensional (2D) simulations (\circ , Fig. 3(f)). Here, the topographical gradient is not simulated explicitly, but instead it is represented by varying the effective lubricant-droplet contact angle $\theta_{ow}(x)$ and the effective lubricant-air contact angle $\theta_{oa}(x)$ ²⁸:

$$\cos \theta_{\alpha}(x) = f_s(x) \cos \theta_{\alpha}^Y + (1 - f_s(x)), \quad (11)$$

where the subscript $\alpha = w, a$ and $\cos \theta_{\alpha}^Y$ is the contact angle on the smooth flat surface. In Fig. 3, few exceptions are present for the 2D simulations, where some of the red data points cross the diagonal line in the phase diagram. This is due to the finite size effect of the lubricant meniscus. As explained in Supplementary Note 1, such a finite size effect becomes relevant for $\tilde{F} \approx 0$ (close to the diagonal line in the phase diagram).

Our experimental results correspond to two different solid surface geometries: stepwise and linear gradients (see Fig. 3(g, h)); and, crucially, show that the direction of motion of a droplet on a given topography can be switched by choosing the interfacial tensions. In Fig. 3, we report experimental results for water droplets and ethylene glycol droplets in contact with different lubricants. In the phase diagram, the hollow and filled symbols correspond to cases where the droplet is encapsulated and not encapsulated by the lubricant, respectively.

To position the experimental data points in the phase diagram, it is necessary to infer the effective wettability of the surface, given by $\cos \theta_{wal,s}^{eff}$ and $\cos \theta_{wal,o}^{eff}$. If the values of $\theta_{wal,s}$, γ_{wa} , γ_{oa} and γ_{ow} are known in the literature²⁹, they can simply be calculated from Eq.

(8). We are able to calculate these for five different droplet-lubricant combinations, as tabulated in Supplementary Note 2. Alternatively, we can determine $\cos \theta_{wal,s}^{eff}$ and $\cos \theta_{wal,o}^{eff}$ using a graphical method as follows. In the vanishing meniscus approximation, the droplet apparent contact angle on the composite solid-lubricant surface can be expressed as^{24,26}

$$\cos \theta_{app} = \frac{\gamma_{(s,o)a} - \gamma_{(s,o)w}}{\gamma_{eff}}, \quad (12)$$

$$= (\cos \theta_{wal,s}^{eff} - \cos \theta_{wal,o}^{eff}) f_s + \cos \theta_{wal,o}^{eff}, \quad (13)$$

$$= \tilde{F} f_s + \cos \theta_{wal,o}^{eff}. \quad (14)$$

As shown in Fig. 4 for seven separate droplet-lubricant pairs, by measuring θ_{app} for different values of the solid fraction f_s , we can determine the normalised driving force \tilde{F} from the gradient of the curve. Furthermore, $\cos \theta_{wal,s}^{eff}$ and $\cos \theta_{wal,o}^{eff}$ can be inferred by extrapolating the curve to $f_s = 1$ and $f_s = 0$. A key advantage of this graphical method is that we can determine \tilde{F} , and hence the direction of droplet motion, without the need to identify the precise wetting states. Droplet self-propulsion can be observed as long as the surface textures are not fully covered by the lubricant. All experimental values of $\cos \theta_{wal,s}^{eff}$, $\cos \theta_{wal,o}^{eff}$ and consequently \tilde{F} used in Fig. 3 are provided in Supplementary Note 2. In all cases, the predicted direction of motion is in agreement with our observation.

It is also useful to estimate the typical driving force experienced by the droplet. Following Eq. (9), the driving force can be written as

$$F \sim \gamma_{eff} \alpha R^2 \tilde{F}. \quad (15)$$

For the linear groove, we typically vary f_s from 0.1 to 0.9 over a sample of 2 cm, leading to $\alpha \sim 40 \text{ m}^{-1}$; while for the stepwise groove, the length scale for the variation in the solid fraction can be taken to be the droplet diameter, $\sim 2 \text{ mm}$, giving $\alpha \sim 400 \text{ m}^{-1}$. Taking typical values for γ_{eff} and \tilde{F} as tabulated in Supplementary Note 2, we find a driving force of the order of 1 – 10 μN for the linear groove and 10 – 100 μN for the stepwise groove.

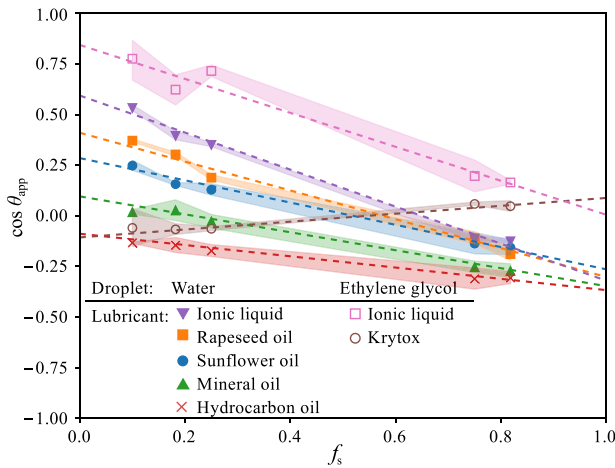


Fig. 4 Estimation of normalised driving force \tilde{F} , as well as contact angles $\theta_{wal,s}^{eff}$ and $\theta_{wal,o}^{eff}$ for water and ethylene glycol droplets on structured surfaces imbibed with various lubricants. Each point is the average of five apparent contact angle θ_{app} measurements of sessile droplets at a given solid fraction f_s . The surrounding coloured area represents the standard deviation. Dashed lines are fits of Eq. (13) using the least-square method. The gradient of the fits corresponds to \tilde{F} , while extrapolations of those fits to $f_s = 1$ and $f_s = 0$ give a measure of the values of the cosine of droplet contact angle on pure solid, $\cos \theta_{wal,s}^{eff}$, and on pure lubricant, $\cos \theta_{wal,o}^{eff}$ respectively.

Discussion

We have reported a spontaneous bidirectional motion of droplet on liquid-infused surfaces with topographical gradients. In contrast to previous studies describing uni-directional droplet motion on surfaces with topographical gradients, here the droplet can move toward the sparser or the denser solid fraction area. We investigated the origin of this bidirectional motion by looking into the relevant surface tension forces acting on the droplet. Our analytical theory predicts, and our simulation and experimental results confirmed, that the direction of the motion is determined by a simple physical quantity, $(\cos \theta_{wal,s}^{eff} - \cos \theta_{wal,o}^{eff})$. This quantity can be intuitively interpreted as preferential wetting of the droplet on the solid majority surface (denser solid area) or on the lubricant majority surface (sparser solid area). The bidirectional motion is also validated over a wide range of surface tension and contact angle combinations, with and without lubricant encapsulation, and for different types of topographical gradients, both in our simulations and experiments.

There are a number of avenues of future work to exploit the novel phenomenon described here. The most immediate question is to better understand the droplet dynamics. In experiments, the observed typical droplet velocity varies over a wide range, from ~ 0.07 to ~ 9.24 mm/s (data provided in Supplementary Note 2). The resulting droplet velocity is due to a complex balance between the driving force due to the texture gradients and the viscous dissipation. Recent studies have shown that there are different contributing mechanisms for viscous dissipation in the droplet and lubricant^{18,27,30–33}. The dominant contributions depend on the viscosity ratio between the droplet and lubricant³¹, the wettability of the lubricant and its meniscus shape³², the amount of excess lubricant²⁷, and the surface texture geometry³³.

It also remains an open problem, which types of topographical gradients are optimal. To illustrate this point, in Supplementary Note 3 we have compared lattice Boltzmann simulation results for droplet motion under (i) a stepwise groove, (ii) and (iii) linear rectangular posts with square and hexagonal arrangements, and (iv) a linear groove. The stepwise groove provides the highest

droplet velocity, but the distance travelled by the droplet is limited. In contrast, the linear groove allows much further droplet displacement but the droplet velocity is slower. In addition, the simulations on the post geometries highlight complex stick-slip droplet motion due to contact line pinning by the surface topography. However, a major advantage of using posts is that we can potentially introduce topographical gradients in two separate directions. Systematic study on different surface textures is an important area for further investigations.

Finally, it is interesting to consider potential applications of the reported bidirectional motion. Since different droplet–lubricant combination may move to different direction, we envisage it can be exploited to sort droplets based on their interfacial properties, and when combined with gravity, simultaneously based on their size and interfacial properties, by playing off the competition between the forces due to wetting gradient and due to gravity. More complex applications include liquid/liquid separation or directing chemical reactions in a droplet microfluidic device.

Methods

Numerical method. Our numerical simulations are carried out employing a ternary free energy lattice Boltzmann method suitable for studying three fluids systems in complex geometries^{32,34}. The free energy model is given by

$$\Psi = \sum_{m=1}^3 \int_{\Omega} \left(\frac{\kappa_m}{2} C_m^2 (1 - C_m)^2 + \frac{\alpha^2 \kappa_m}{2} (\nabla C_m)^2 \right) dV - \sum_{m=1}^3 \int_{\partial\Omega} h_m C_m dS, \quad (16)$$

where C_m is the concentration of fluid phase m . In our simulations, $m = 1, 2, 3$ represent the droplet, gas and lubricant phases, respectively. The simulation parameters α , κ and h_m are used to tune the interfacial thermodynamics of the system. Specifically, α and κ determine the interface width and surface tension between the fluid phases. The h_m parameters are related to the intrinsic contact angles of the fluids with the solid. Supplementary Methods provide additional details on how these parameters are chosen.

In the following, we set the local fluid density to be uniform, i.e., $\rho = C_1 + C_2 + C_3 = 1$, since we expect that the effect of inertia is negligible for the droplet motion. Alternative simulation schemes are available for situations where the density difference between the fluid phases is important^{35,36}. Then, introducing the order parameters $\phi \equiv C_1 - C_2$, and $\psi \equiv C_3$, we can solve the fluid equations of motion corresponding to the continuity, Navier–Stokes, and two Cahn–Hilliard equations

$$\partial_t \rho + \nabla \cdot (\rho \vec{v}) = 0, \quad (17)$$

$$\partial_t (\rho \vec{v}) + \nabla \cdot (\rho \vec{v} \otimes \vec{v}) = -\nabla \cdot \mathbf{P} + \nabla \cdot [\eta (\nabla \vec{v} + \nabla \vec{v}^T)], \quad (18)$$

$$\partial_t \phi + \nabla \cdot (\phi \vec{v}) = M_{\phi} \nabla^2 \mu_{\phi}, \quad (19)$$

$$\partial_t \psi + \nabla \cdot (\psi \vec{v}) = M_{\psi} \nabla^2 \mu_{\psi}, \quad (20)$$

where \vec{v} and η are the fluid velocity and viscosity, respectively. Equations (19) and (20) describe the evolution of ϕ and ψ , and, correspondingly, the interfaces between the three fluids. The thermodynamic properties of the system, described in the free energy model in Eq. (16), enter the equations of motion via the chemical potentials, $\mu_q = \delta \Psi / \delta q$, ($q = \phi$ and ψ), and the pressure tensor, \mathbf{P} , defined by $\partial_{\beta} P_{\alpha\beta} = \phi \partial_{\alpha} \mu_{\phi} + \psi \partial_{\alpha} \mu_{\psi}$. The equations of motion in Eqs. (17)–(20) are solved using the lattice Boltzmann method^{34,37}.

As discussed in the “Results” section, we have carried out three different types of simulation geometries. It is worth noting that, in the full and quasi 3D simulations, the driving force for droplet motion arises due to gradient in the surface textures. If there is no topographical gradient, the droplet is stationary. In the 2D simulations, however, since we do not explicitly simulate the surface texture, we introduce wetting gradients and hence the driving force for droplet motion by varying the lubricant–droplet and lubricant–air contact angles via the h_m parameters in Eq. (16).

Experimental method. For the experiments, we use photolithography to produce surfaces with 60 μm deep grooves in the x -direction. The width of each groove can be tuned (between 10 and 75 μm) to obtain solid fractions f_s ranging from 0.1 to 0.9. This allows us to create topographical gradients along the x -direction by continuously increasing or decreasing the width of the grooves. The typical sample size is 2 cm long

and 1 cm wide. After fabrication, the geometry of the surfaces is carefully measured using optical profilometry and SEM (scanning electron microscope) imaging.

To reduce the contact angle hysteresis that would hinder droplet motion, the structured surfaces are treated with SOCAL (Slippery Omniphobic Covalently Attached Liquid), following the protocol from Wang et al.³⁸, modified for SU-8 substrates (see Supplementary Methods for details). We verify the SOCAL coating by measuring the contact angle ($104^\circ \pm 2^\circ$) and contact angle hysteresis ($<5^\circ$) of a water droplet deposited on a non-structured (flat) region of the sample.

The surfaces are then dipped in a lubricant and left to drain vertically for 10 min, in order to fill the grooves and create a liquid-infused surface. Droplets are finally deposited on the imbibed surfaces using a thin needle and their motion is tracked using a camera placed on the side. The volume of the liquid droplets used in the experiments is 5 μ l, with typical droplet base diameter ≈ 2 mm. When placed on the substrate, the droplet is approximately sitting on top of 30 stripes. To rule out the effect of gravity on the droplet motion, the surface is slightly tilted ($\approx 0.5^\circ$) against the direction of motion. The procedure is repeated five times for each configuration to ensure reproducibility.

Data availability

The datasets generated during and/or analysed during the current study are available from the corresponding author on reasonable request.

Code availability

The ternary lattice Boltzmann code used in the current study are available from the corresponding author on reasonable request.

Received: 9 April 2020; Accepted: 11 August 2020;

Published online: 21 September 2020

References

1. Cho, S. K., Moon, H. & Kim, C.-J. Creating, transporting, cutting, and merging liquid droplets by electrowetting-based actuation for digital microfluidic circuits. *J. Microelectromech. Syst.* **12**, 70–80 (2003).
2. Li, X.-M., Reinhoudt, D. & Crego-Calama, M. What do we need for a superhydrophobic surface? A review on the recent progress in the preparation of superhydrophobic surfaces. *Chem. Soc. Rev.* **36**, 1350–1368 (2007).
3. Willmott, G. R., Neto, C. & Hendy, S. C. Uptake of water droplets by non-wetting capillaries. *Soft Matter* **7**, 2357–2363 (2011).
4. Damak, M. & Varanasi, K. K. Electrostatically driven fog collection using space charge injection. *Sci. Adv.* **4**, eaao5323 (2018).
5. Labbé, R. & Duprat, C. Capturing aerosol droplets with fibers. *Soft Matter* **15**, 6946–6951 (2019).
6. Sun, Q. et al. Surface charge printing for programmed droplet transport. *Nat. Mater.* **18**, 936–941 (2019).
7. Chaudhury, M. K. & Whitesides, G. M. How to make water run uphill. *Science* **256**, 1539–1541 (1992).
8. Varnik, F. et al. Wetting gradient induced separation of emulsions: a combined experimental and lattice Boltzmann computer simulation study. *Phys. Fluids* **20**, 072104 (2008).
9. Reyssat, M., Pardo, F. & Quéré, D. Drops onto gradients of texture. *Europhys. Lett.* **87**, 36003 (2009).
10. Moradi, N., Varnik, F. & Steinbach, I. Roughness-gradient-induced spontaneous motion of droplets on hydrophobic surfaces: a lattice Boltzmann study. *Europhys. Lett.* **89**, 26006 (2010).
11. Li, J. et al. Oil droplet self-transportation on oleophobic surfaces. *Sci. Adv.* **2**, e1600148 (2016).
12. Style, R. W. et al. Patterning droplets with durotaxis. *Proc. Natl Acad. Sci. U.S.A.* **110**, 12541–12544 (2013).
13. Zhang, C. et al. Bioinspired pressure-tolerant asymmetric slippery surface for continuous self-transport of gas bubbles in aqueous environment. *ACS Nano* **12**, 2048–2055 (2018).
14. McCarthy, J., Vella, D. & Castrejón-Pita, A. A. Dynamics of droplets on cones: self-propulsion due to curvature gradients. *Soft Matter* **15**, 9997–10004 (2019).
15. Launay, G. et al. Self-propelled droplet transport on shaped-liquid surfaces. <https://arxiv.org/abs/1908.01305> (2019).
16. Wong, T.-S. et al. Bioinspired self-repairing slippery surfaces with pressure-stable omniphobicity. *Nature* **477**, 443–447 (2011).
17. Lafuma, A. & Quéré, D. Slippery pre-suffused surfaces. *Europhys. Lett.* **96**, 56001 (2011).
18. Smith, J. D. et al. Droplet mobility on lubricant-impregnated surfaces. *Soft Matter* **9**, 1772–1780 (2013).
19. Juuti, P. et al. Achieving a slippery, liquid-infused porous surface with anti-icing properties by direct deposition of a synthesized aerosol nanoparticles on a thermally fragile substrate. *Appl. Phys. Lett.* **110**, 161603 (2017).
20. Weisensee, P. B. et al. Condensate droplet size distribution on lubricant-infused surfaces. *Int. J. Heat. Mass Transf.* **109**, 187–199 (2017).
21. Villegas, M., Zhang, Y., Abu Jarad, N., Soleymani, L. & Didar, T. F. Liquid-infused surfaces: a review of theory, design, and applications. *ACS Nano* **13**, 8517–8536 (2019).
22. Young, T. III An essay on the cohesion of fluids. *Philos. Trans. R. Soc. Lond.* **95**, 65–87 (1805).
23. Subramanian, R. S., Moumen, N. & McLaughlin, J. B. Motion of a drop on a solid surface due to a wettability gradient. *Langmuir* **21**, 11844–11849 (2005).
24. Sempregon, C., McHale, G. & Kusumaatmaja, H. Apparent contact angle and contact angle hysteresis on liquid-infused surfaces. *Soft Matter* **13**, 101–110 (2017).
25. Kreder, M. J. et al. Film dynamics and lubricant depletion by droplets moving on lubricated surfaces. *Phys. Rev. X* **8**, 031053 (2018).
26. McHale, G., Orme, B. V., Wells, G. G. & Ledesma-Aguilar, R. Apparent contact angles on lubricant-impregnated surfaces/SLIPS: From superhydrophobicity to electrowetting. *Langmuir* **35**, 4197–4204 (2019).
27. Daniel, D., Timonen, J. V. I., Li, R., Velling, S. J. & Aizenberg, J. Oleoplaning droplets on lubricated surfaces. *Nat. Phys.* **13**, 1020–1025 (2017).
28. Cassie, A. B. D. & Baxter, S. Wettability of porous surfaces. *Trans. Faraday Soc.* **40**, 546–551 (1944).
29. Girifalco, L. & Good, R. A theory for the estimation of surface and interfacial energies. I. Derivation and application to interfacial tension. *J. Phys. Chem.* **61**, 904–909 (1957).
30. Mistura, G. & Pierno, M. Drop mobility on chemically heterogeneous and lubricant-impregnated surfaces. *Adv. Phys.* **2**, 591–607 (2017).
31. Keiser, A., Keiser, L., Clanet, C. & Quéré, D. Drop friction on liquid-infused materials. *Soft Matter* **13**, 6981–6987 (2017).
32. Sadullah, M. S., Sempregon, C. & Kusumaatmaja, H. Drop dynamics on liquid-infused surfaces: the role of the lubricant ridge. *Langmuir* **34**, 8112–8118 (2018).
33. Keiser, L., Keiser, A., L'Estimé, M., Bico, J. & Reyssat, É. Motion of viscous droplets in rough confinement: paradoxical lubrication. *Phys. Rev. Lett.* **122**, 074501 (2019).
34. Sempregon, C., Krüger, T. & Kusumaatmaja, H. Ternary free-energy lattice Boltzmann model with tunable surface tensions and contact angles. *Phys. Rev. E* **93**, 033305 (2016).
35. Wöhrwag, M., Sempregon, C., Mazloomi-Moqaddam, A., Karlin, I. & Kusumaatmaja, H. Ternary free-energy entropic lattice Boltzmann model with a high density ratio. *Phys. Rev. Lett.* **120**, 234501 (2018).
36. Bala, N., Pepona, M., Karlin, I., Kusumaatmaja, H. & Sempregon, C. Wetting boundaries for a ternary high-density-ratio lattice Boltzmann method. *Phys. Rev. E* **100**, 013308 (2019).
37. Briant, A. J. & Yeomans, J. M. Lattice Boltzmann simulations of contact line motion. II. Binary fluids. *Phys. Rev. E* **69**, 031603 (2004).
38. Wang, L. & McCarthy, T. Covalently attached liquids: instant omniphobic surfaces with unprecedented repellency. *Angew. Chem.* **128**, 252 (2015).

Acknowledgements

M.S.S. is supported by an LPDP (Lembaga Pengelola Dana Pendidikan) scholarship from the Indonesian Government. H.K. acknowledges funding from EPSRC (grant EP/P007139/1) and Procter and Gamble. G.G.W. and G.L. acknowledge funding from EPSRC (grant EP/P026613/1).

Author contributions

H.K., G.W., R.L.A. designed the research and supervised the project. M.S.S., J.P. and H.K. developed the theory and carried out the simulations. G.L. and G.W. performed the experiments. Y.G. and G.M. contributed in the interpretation of the results. H.K. and M.S.S. drafted the manuscript, with all authors contributing to the writing of the manuscript.

Competing interests

The authors declare no competing interests.

Additional information

Supplementary information is available for this paper at <https://doi.org/10.1038/s42005-020-00429-8>.

Correspondence and requests for materials should be addressed to H.K.

Reprints and permission information is available at <http://www.nature.com/reprints>

Publisher's note Springer Nature remains neutral with regard to jurisdictional claims in published maps and institutional affiliations.



Open Access This article is licensed under a Creative Commons Attribution 4.0 International License, which permits use, sharing, adaptation, distribution and reproduction in any medium or format, as long as you give appropriate credit to the original author(s) and the source, provide a link to the Creative Commons license, and indicate if changes were made. The images or other third party material in this article are included in the article's Creative Commons license, unless indicated otherwise in a credit line to the material. If material is not included in the article's Creative Commons license and your intended use is not permitted by statutory regulation or exceeds the permitted use, you will need to obtain permission directly from the copyright holder. To view a copy of this license, visit <http://creativecommons.org/licenses/by/4.0/>.

© The Author(s) 2020